materials

MDPI

Article

Ce Filling Limit and Its Influence on Thermoelectric Performance of Fe_3CoSb_{12}-Based Skutterudite Grown by a Temperature Gradient Zone Melting Method

Xu-Guang Li [1,†], Wei-Di Liu [2,3,†], Shuang-Ming Li [1,*], Dou Li [1], Jia-Xi Zhu [1], Zhen-Yu Feng [1], Bin Yang [1], Hong Zhong [1], Xiao-Lei Shi [3,4] and Zhi-Gang Chen [3,4,*]

1 State Key Laboratory of Solidification Processing, Northwestern Polytechnical University, Xi'an 710072, China; leexuguang@mail.nwpu.edu.cn (X.-G.L.); lidou@mail.nwpu.edu.cn (D.L.); zhujx1107@mail.nwpu.edu.cn (J.-X.Z.); fengzhenyu97@mail.nwpu.edu.cn (Z.-Y.F.); 2016100413yb@mail.nwpu.edu.cn (B.Y.); zhonghong123@nwpu.edu.cn (H.Z.)
2 Australian Institute of Bioengineering and Nanotechnology, The University of Queensland, Brisbane, QLD 4072, Australia; weidi.liu@uq.net.au
3 Centre for Future Materials, University of Southern Queensland, Brisbane, QLD 4300, Australia; xiaolei.shi@usq.edu.au
4 School of Mechanical and Mining Engineering, The University of Queensland, Brisbane, QLD 4072, Australia
* Correspondence: lsm@nwpu.edu.cn (S.-M.L.); zhigang.chen@usq.edu.au (Z.-G.C.)
† These authors contributed equally to this work.

check for updates

Citation: Li, X.-G.; Liu, W.-D.; Li, S.-M.; Li, D.; Zhu, J.-X.; Feng, Z.-Y.; Yang, B.; Zhong, H.; Shi, X.-L.; Chen, Z.-G. Ce Filling Limit and Its Influence on Thermoelectric Performance of Fe_3CoSb_{12}-Based Skutterudite Grown by a Temperature Gradient Zone Melting Method. *Materials* **2021**, *14*, 6810. https://doi.org/10.3390/ma14226810

Academic Editor: Joseph Poon

Received: 25 September 2021
Accepted: 9 November 2021
Published: 11 November 2021

Abstract: $CoSb_3$-based skutterudite is a promising mid-temperature thermoelectric material. However, the high lattice thermal conductivity limits its further application. Filling is one of the most effective methods to reduce the lattice thermal conductivity. In this study, we investigate the Ce filling limit and its influence on thermoelectric properties of p-type Fe_3CoSb_{12}-based skutterudites grown by a temperature gradient zone melting (TGZM) method. Crystal structure and composition characterization suggests that a maximum filling fraction of Ce reaches 0.73 in a composition of $Ce_{0.73}Fe_{2.73}Co_{1.18}Sb_{12}$ prepared by the TGZM method. The Ce filling reduces the carrier concentration to 1.03×10^{20} cm^{-3} in the $Ce_{1.25}Fe_3CoSb_{12}$, leading to an increased Seebeck coefficient. Density functional theory (DFT) calculation indicates that the Ce-filling introduces an impurity level near the Fermi level. Moreover, the rattling effect of the Ce fillers strengthens the short-wavelength phonon scattering and reduces the lattice thermal conductivity to 0.91 W m^{-1} K^{-1}. These effects induce a maximum Seebeck coefficient of 168 μV K^{-1} and a lowest κ of 1.52 W m^{-1} K^{-1} at 693 K in the $Ce_{1.25}Fe_3CoSb_{12}$, leading to a peak zT value of 0.65, which is 9 times higher than that of the unfilled Fe_3CoSb_{12}.

Keywords: skutterudite; $CoSb_3$; Ce-filling; thermoelectric

1. Introduction

With the consumption of traditional fossil fuels and the aggravation of environment pollution, exploring new and effective energy utilization techniques has experienced increasing significance [1–3]. Thermoelectric technology, enabling the direct energy conversion between heat and electricity, has provided a promising and eco-friendly energy solution [4–6]. The thermoelectric performance is fundamentally characterized by the material dimensionless figure-of-merit (zT), defined as $zT = S^2\sigma T/\kappa$, where S, σ, κ and T are the Seebeck coefficient, electrical conductivity, thermal conductivity (comprised of electronic contribution κ_e and lattice contribution κ_l) and temperature in Kelvin, respectively [7–9]. High power factor ($S^2\sigma$) and low κ are necessary for high zT [8,9]. S, σ, and κ_e are related to each other as a function of other fundamental parameters, such as carrier concentration (n) [10–12]. These fundamental parameters need to be optimized. Typically, the n of thermoelectric materials can be optimized by valence electron counts engineering [13,14],

modulation doping [15], and band gap engineering [16]. Other than the interrelated parameters, reducing κ_l can achieve a low κ and high zT [17]. The reduced κ_l can be achieved by introducing additional structure defects, such as point defects [18], dense grain boundaries [19], and nanoprecipitates [20,21] for strengthening phonon scattering.

Among thermoelectric materials, skutterudites, especially $CoSb_3$-based skutterudites, are promising application prospect in the field of mid-temperature power generation [22–24]. Binary $CoSb_3$ is an intermetallic compound formed by a peritectic reaction [25]. $CoSb_3$ is a body-centered cubic cage-like crystal structure (*Im-3* space group) with two void positions at the 2a sites (0, 0, 0) and (1/2, 1/2, 1/2) in the unit cell [26,27]. Intrinsic $CoSb_3$ is a p-type semiconductor with high S and high carrier mobility (μ) [28]. However, the strong Co-Sb covalent bonding induces high κ_l (~7.5 W m^{-1} K^{-1} at room temperature) of intrinsic $CoSb_3$, limiting its thermoelectric performance [29,30].

To reduce the κ_l of intrinsic $CoSb_3$, filling the void position at the 2a site with small atom can tune $CoSb_3$ into filled-$CoSb_3$ ($R_xCo_4Sb_{12}$, R is the filling elements and x is the filling fraction), which possesses a feature of phonon glass and electron crystal (PGEC) [31]. The fillers are loosely bounded and rattle near the equilibrium positions and significantly scatter the low-frequency phonons, leading to decreased κ_l and improved zT [32,33]. The fillers can be rare-earth atoms [18,34], alkaline-earth atoms [35], alkaline metals atoms [36]. Pei et al. [36] found that n-type $Na_{0.48}Co_4Sb_{12}$ had a reduced room-temperature κ_l of 3.5 W m^{-1} K^{-1} in accordance with a peak zT of 1.25. Alkaline-earth Ba can be filled into the void position at the 2a site of $CoSb_3$ to form n-type filled-$CoSb_3$ and approach a decreased κ_l of 0.73 W m^{-1} K^{-1} and a peak zT of ~1.0 in $Ba_{0.51}CO_4Sb_{12}$ [35]. Yb is another utilized rare-earth filler since the relatively high atomic mass and small ionic radius [18,37], which can lead to a low κ_l of 0.62 W m^{-1} K^{-1} in n-type $Yb_{0.47}Co_4Sb_{12}$ [38]. However, rare-earth Ce has a low filling fraction in $CoSb_3$ comparing with Yb. Morelli et al. [39] prepared n-type Ce-filled $CoSb_3$ by arc melting and found a low filling fraction of ~0.1. Even though with a low Ce filling fraction, the κ_l was strongly depressed and a low κ_l of ~4 W m^{-1} K^{-1} was obtained, which is only half of the unfilled $CoSb_3$. To improve the Ce filling fraction in undoped $CoSb_3$, Tang et al. [40] used phase diagram method to increase this value up to 0.2. Due to the increased filling fraction, a further reduced κ_l of ~2 W m^{-1} K^{-1} and a zT value of 1.3 at 850 K were obtained in n-type $Ce_{0.14}Co_4Sb_{12}$ prepared by melting-quenching-annealed-sintering. Besides, the thin film $CoSb_3$ sample prepared by deposition experienced increased Ce-filling fraction. Smalley et al. [41] reported a high Ce-filling fraction of ~0.55 in deposited $CoSb_3$ film.

Although heavy filling in the void position remarkably reduces the κ_l of $CoSb_3$-based thermoelectric materials, heavily filled $CoSb_3$-based materials are generally n-type semiconductors because the fillers function as electron donors [20,34,41]. In term of the assembly of thermoelectric devices, both p-type and n-type materials are required. Hence, p-type $CoSb_3$-based thermoelectric materials are necessary. To achieve low κ_l of p-type $CoSb_3$-based thermoelectric materials, Fe has been partially used to substitute Co [6,18,40], behaving as the electron acceptor to tune into p-type. Particularly, after Fe substitution at the Co site, $CaFe_{3.5}Co_{0.5}Sb_{12}$ has a high $S^2\sigma$ of 33 μW cm^{-1} K^{-2} with a positive S of 170 μV K^{-1} and a low κ_l of ~0.9 W m^{-1} K^{-1} at 773 K [42]. Furthermore, charge-compensational doping by the substitution at Co or Sb sites has been widely applied to increase the filling faction of Ce in bulk $CoSb_3$-based skutterudites, which can simultaneously tune n-type $CoSb_3$ skutterudites into p-type ones [43,44]. Tanahashi et al. [45] found a Ce filling fraction of ~0.9 in p-type $CoSb_3$-based skutterudites with the nominal composition of $CeFe_3CoSb_{12}$, which is prepared by gas-phase atomization and sintering and approached a zT of 0.63 at 700 K. Chen et al. [46] reported a p-type $Ce_{0.95}Fe_3CoSb_{12.1}$ grown by scanning laser melting method combined with spark plasma sintering and achieved the Ce filling fraction of 0.85 and the zT of ~0.79 at 750 K.

As suggested in Figure 1a–f, crystal structures of the unfilled and Ce-filled Fe_3CoSb_{12} and corresponding density functional theory (DFT)-calculated band structures and density of states (DOS) were firstly investigated. As can be seen, Ce-filling introduces an impurity

level near the Fermi energy (E_F), which is mainly contributed by the *f* orbital of Ce atom. Besides, Ce-filling also increases the slope of DOS near E_F and correspondingly contributes to increased *S* [47,48]. Additionally, filled $CoSb_3$-based thermoelectric materials can be fabricated by various methods, such as traditional melting-quenching-annealing-sintering [49], melt-spinning combined with spark plasma sintering technique (MS-SPS) [50], high-energy ball-milling combined with hot pressing (BM-HP) technique [51], and temperature gradient zone melting (TGZM) method [52,53]. Among them, TGZM is a novel material preparation method, which can synthesize $CoSb_3$-based skutterudites with faster speed and higher purity by avoiding the complex peritectic solidification process. Effects of Ce fillers and its filling fraction in TGZM-prepared Fe_3CoSb_{12} might be different from that prepared by other methods. In this study, we employed the novel TGZM method to investigate the influence and filling fraction of Ce in Fe_3CoSb_{12}. A series of Ce-filled p-type $Ce_xFe_3CoSb_{12}$ (x = 0 to 1.5) samples were prepared. We found that the maximum filling level of Ce is 0.73 in the TGZM-prepared $Ce_{1.25}Fe_3CoSb_{12}$ with a measured composition of $Ce_{0.73}Fe_{2.73}Co_{1.18}Sb_{12}$. The synergistic effect on Fe substitution at the Co and Ce-filling result in reduced n_H to 1.03×10^{20} cm^{-3} in $Ce_{1.25}Fe_3CoSb_{12}$. A low κ_l of 0.91 W m^{-1} K^{-1} at 693 K can be obtained in the $Ce_{1.25}Fe_3CoSb_{12}$, significantly contributing to an increased *zT* of 0.65 at 693 K.

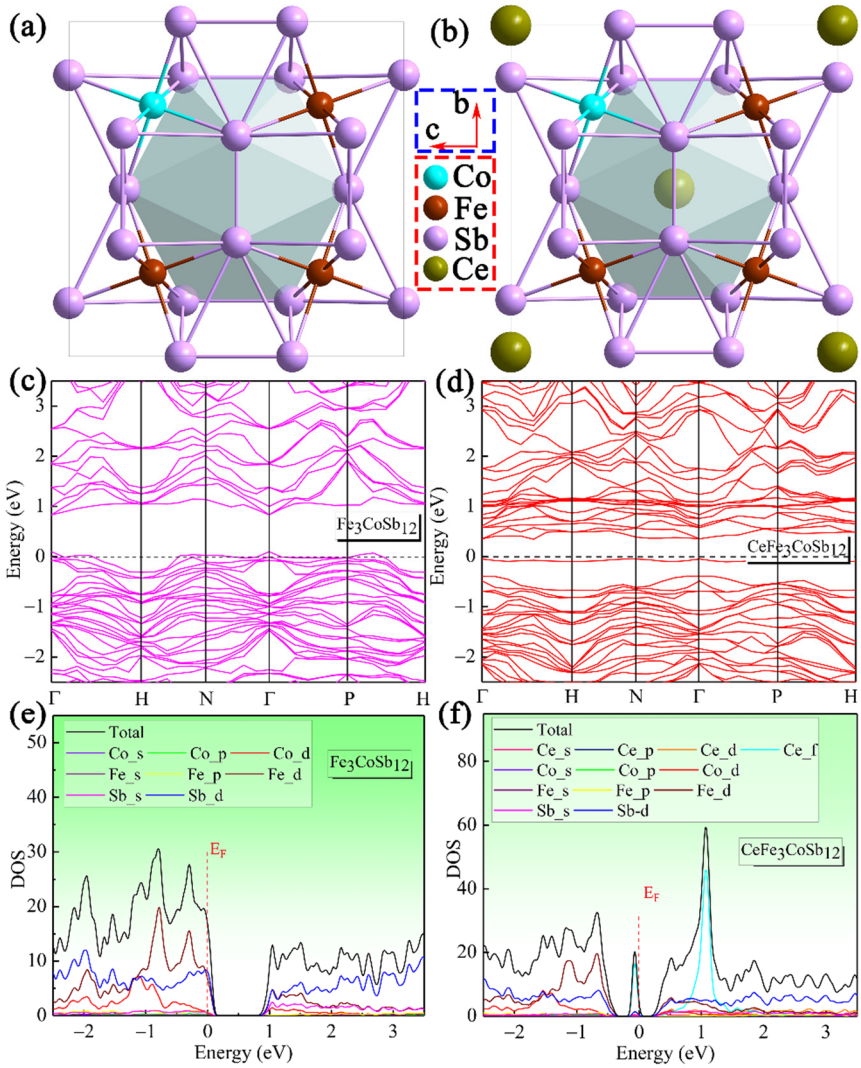

Figure 1. Band structures and density of states (DOS) of the unfilled and Ce-filled Fe_3CoSb_{12}-based skutterudites: The conventional unit cell of unfilled (**a**) and Ce-filled (**b**) Fe_3CoSb_{12}-based skutterudites. Calculated band structures of unfilled (**c**) and Ce-filled (**d**) Fe_3CoSb_{12}-based skutterudites and Calculated DOS of unfilled (**e**) and Ce-filled (**f**) Fe_3CoSb_{12}-based skutterudites.

2. Materials and Methods

2.1. Samples Preparation

Initial ingots of (Fe_3Co)-95 at. % Sb filled with x at. % Ce (x = 0, 0.25, 0.5, 0.75, 1, 1.25, 1.5) were prepared by induction melting at 1473 K for 30 min in a vacuum induction furnace (Xi'an, China) (~10^{-3}Pa) followed by a furnace cooling. Elements Fe (99.95 at. %), Co (99.95 at. %), Sb (99.995 at. %), and Ce (99.9%), purchased from CNBM (Chengdu, China) Optoelectronic Materials Com., Ltd., were properly weighed as raw materials according to the nominal compositions. Extra Sb was added to obtain the samples of nominal composition $Ce_xFe_3CoSb_{12}$ after the TGZM process. Besides, extra Ce was introduced to compensate the Ce loss during TGZM process. The as-cast ingots were cut into cylinder samples with a diameter of 12.8 mm, and the oxide layer on the surface was cleaned before being put into a high-purity alumina tube with an inner diameter of 13 mm to execute the TGZM process, which was described in detail in previous reports [54,55]. The TGZM process was then conducted in a homemade directional solidification furnace of a thermal stabilization time of 48 h with an estimated temperature gradient of 40 K/mm. The TGZM-grown samples were obtained from the mushy zone formed during the TGZM process. The obtained samples were cleaned, polished, and carried out microstructure characterization and performance tests. Samples throughout the manuscript are described as their nominal compositions after the TGZM process.

2.2. Microstructure Characterization

The crystal structures of as-fabricated samples were determined by powder X-ray diffraction (XRD-7000, Shimadzu, Japan) with Cu-K_α radiation. The lattice parameters were obtained by Rietveld analysis. Scanning electron microscopy (SEM, Verios G4, FEI, equipped with EDS, Hillsboro, OR, USA) was used to acquire the morphologies of the sample's surface and a Double Cs Corrector Transmission Electron Microscope (Cs-TEM, Themis Z, FEI, Hillsboro, OR, USA) was used to characterize their microstructure and chemical features. The actual chemical content was obtained by taking the average of fifteen different positions of each sample. Electron backscattered diffraction (EBSD, Thermo QuasOr type, Waltham, MA, USA) attached to FEI Helios G4 CX type SEM (Hillsboro, OR, USA)was used to determine the crystal orientation relationship.

2.3. Properties Measurements

The samples with 12.7 mm in diameter and 1.5 mm in thickness were used to measure their thermoelectric properties from 303 K to 813 K. In our measurements, σ and S were measured simultaneously using the LSR-3 system (Linseis, Zelb, Bavaria, Germany) under the helium atmosphere. κ was calculated by $\kappa = D \cdot C_P \cdot \rho$, where D is the thermal diffusivity measured by LFA-1000 (Linseis, Zelb, Bavaria, Germany), C_P the specific heat obtained by DSC (STA-449C, Netzsch, Germany), and ρ the density obtained by the Archimedes method. The Hall coefficient (R_H), measured on the PPMS system (CFMS-14T, London, UK) with a magnetic field of ±2T, was used to calculate the room-temperature Hall carrier concentration (n_H), determined by the formula [18]: $n_H = 1/eR_H$, where e represents the electron charge.

2.4. Density Functional Theory (DFT) Calculations

The physical properties of Fe_3CoSb_{12}, $CeFe_3CoSb_{12}$ were calculated using the Cambridge Serial Total Energy Package (CASTEP) [56]. The exchange-correlation interactions were described using the generalized gradient approximation (GGA) with the Perdew-Burke-Ernzerhof (PBE) type [57]. The plane wave cutoff energy was 450 eV for geometry optimization, band structures, and density of states calculations. The Monkhorst-Pack grid parameters were set to 8 × 8 × 8 (34 Irreducible k-points) for calculations. The Convergence tolerances were set to 1.0 × 10^{-5} eV/atom, 0.03 eV/Å, 0.05 GPa and 0.001 Å for energy, maximum force, maximum stress and maximum displacement, respectively.

3. Results and Discussion

3.1. Microstructure and Phase Composition

To understand crystal structures of the as-prepared $Ce_xFe_3CoSb_{12}$ (x = 0 to 1.5), we firstly investigated powder X-ray diffraction (XRD) patterns and the results are shown in Figure 2a. Main diffraction peaks of samples can be identified as the body-centered cubic $CoSb_3$ with a lattice parameter *a* of 9.034 Å and a space group of *Im-3* (JCPDS 19-0336). Due to the characteristic of eutectic reaction, a small number of Sb impurities are observed. Figure 2b plots the corresponding *a* of the as-prepared $Ce_xFe_3CoSb_{12}$ (x = 0 to 1.5). The calculated *a* increases with increasing the Ce-filling content and stabilizes at the x of 1.25. The increased *a* should be attributed to Ce-filling induced lattice expansion. TEM investigations were carried out to further understand the crystal structure of the as-fabricated $Ce_xFe_3CoSb_{12}$. Figure 2c is an atomic-resolution TEM high-angle annular dark-field (HAADF) image of $CeFe_3CoSb_{12}$. The inset of Figure 2c is superimposed a 2 × 2 × 2 supper cell model for the $CeFe_3CoSb_{12}$ along the [100] direction, well-matched with the observed lattice. Figure 2d is a selected area electron diffraction (SAED) pattern and can be indexed along the [100] zone-axis. Figure 2e presents the corresponding inverse Fast Fourier transform (IFFT) image along with the (011) planes. The observed *d* spacing between (011) planes is ~6.64 Å, which is larger than that of $CoSb_3$ (~6.39 Å). Besides, no obvious lattice distortion can be observed from Figure 2e, indicating that the as-fabricated samples have a high crystallinity. Figure 2f–h show the EBSD inverse pole figure (IPF) maps of the $Ce_{1.25}Fe_3CoSb_{12}$. As can be seen, no obvious texture information can be observed, indicating the isotropic thermoelectric performance of the as-fabricated $Ce_xFe_3CoSb_{12}$.

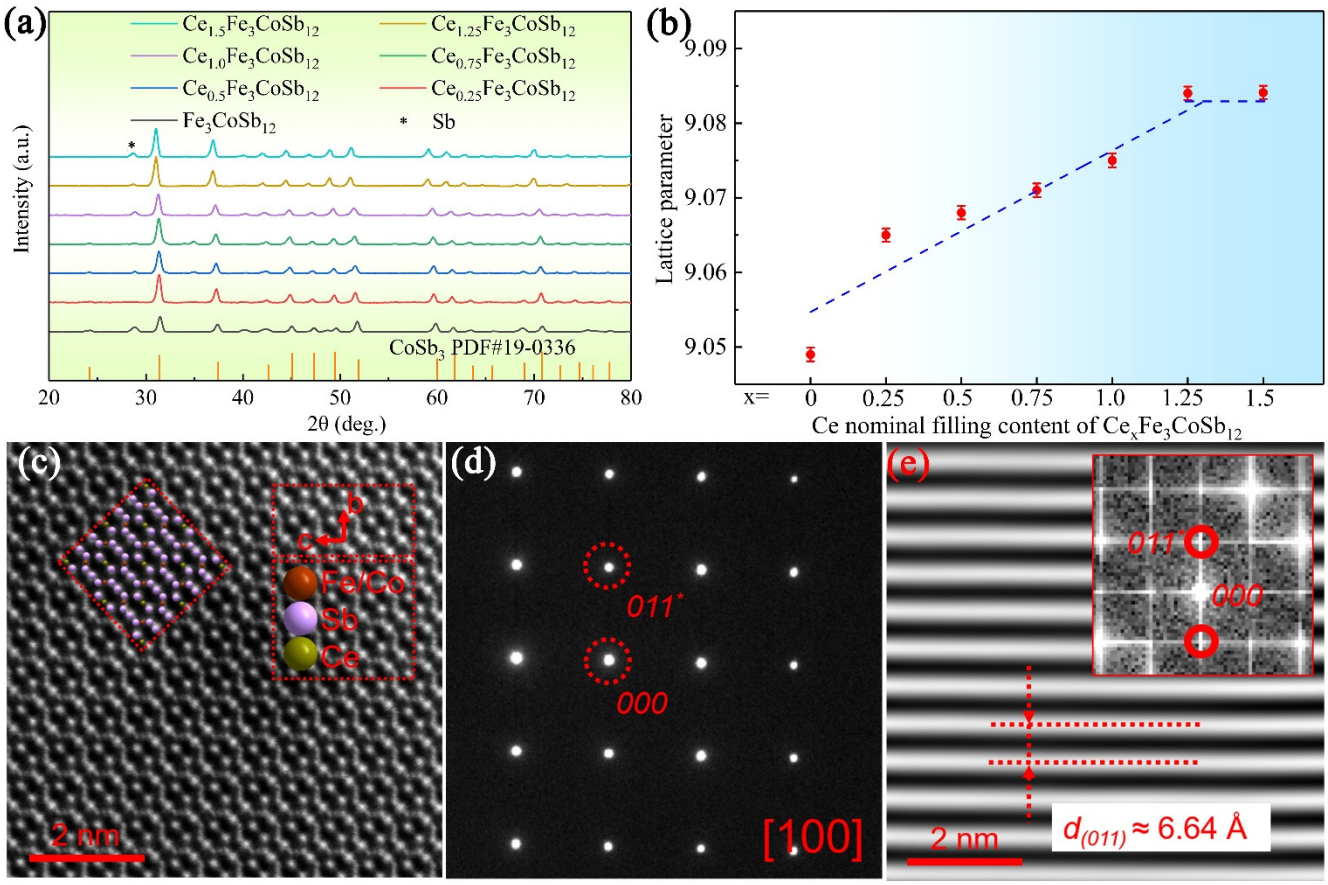

Figure 2. *Cont.*

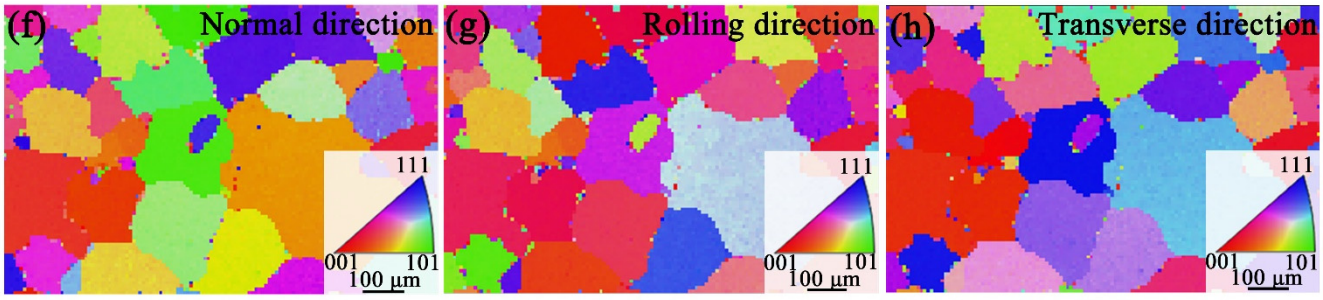

Figure 2. (**a**) XRD diffraction patterns and (**b**) Lattice parameter *a* of the as-prepared $Ce_xFe_3CoSb_{12}$ (x = 0 to 1.5). (**c**) HAADF image with an inserted 2 × 2 × 2 supper cell model, (**d**) SAED pattern in (**c**) and (**e**) Inverse pole figure (IPF) maps in $CeFe_3CoSb_{12}$. The EBSD IPF maps in (**f**) normal direction, (**g**) rolling direction and (**h**) transverse direction of the $Ce_{1.25}Fe_3CoSb_{12}$.

To understand the composition of the as-fabricated $Ce_xFe_3CoSb_{12}$, we conducted SEM image and the corresponding EDS maps of the $Ce_{1.25}Fe_3CoSb_{12}$ and the results are shown in Figure 3a–e. As can be seen, Fe, Co, Sb, and Ce are evenly distributed in the as-fabricated $Ce_{1.25}Fe_3CoSb_{12}$. A typical high-resolution TEM (HRTEM) HAADF image of the $CeFe_3CoSb_{12}$ is shown in Figure 3f. Figure 3g–i are the corresponding elemental maps in atomic scale. Figure 3j is a magnified overlap of elemental maps where the dark green balls represent Ce fillers. As can be seen, Ce filler sits at the 2a sites in the cage among the Sb-icosahedron (pink ball).

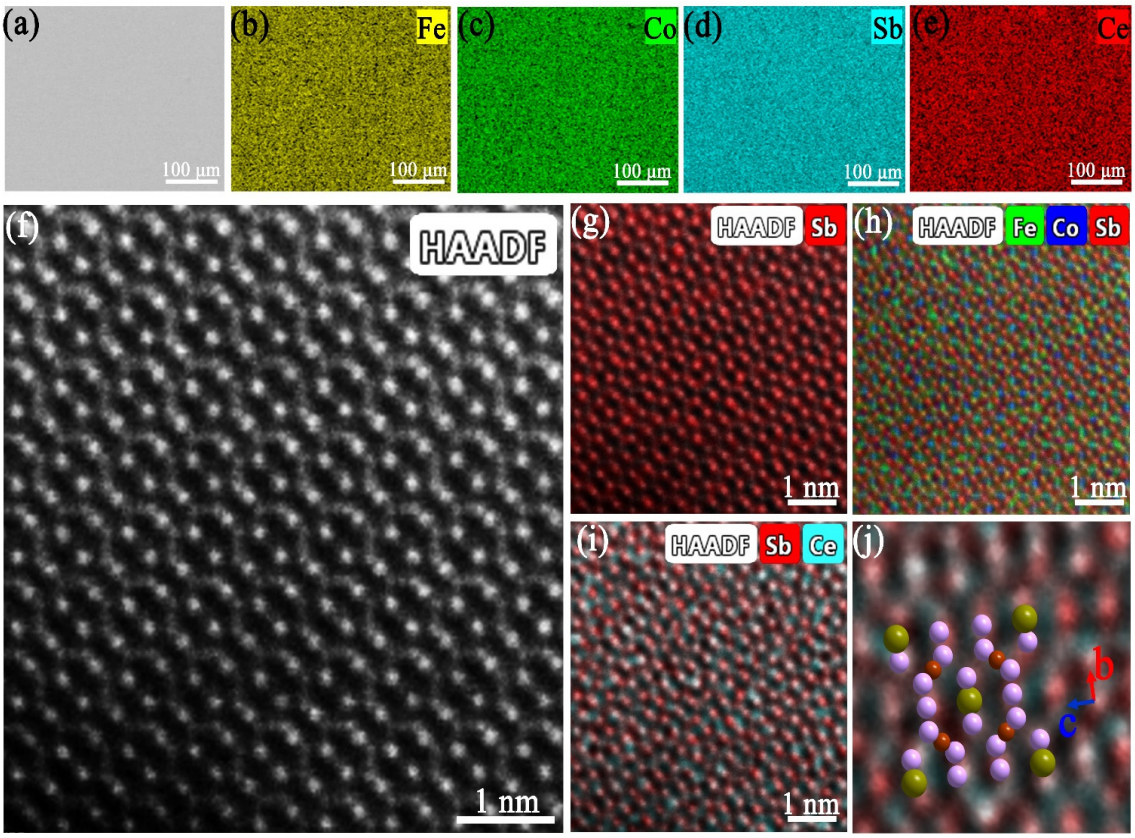

Figure 3. SEM image (**a**), the corresponding elemental maps of Fe (**b**), Co (**c**), Sb (**d**), Ce (**e**) of the $Ce_{1.25}Fe_3CoSb_{12}$ sample. The HRTEM HAADF image (**f**) of the $CeFe_3CoSb_{12}$ and the corresponding atomic scale elemental map of Sb (**g**), overlay elemental map of Fe, Co and Sb (**h**), overlay elemental map of Sb and Ce (**i**), the magnified overlap of elemental maps superimposed with the crystal structure (**j**), where the dark green ball, the pink ball and dull-red ball represent Ce, Sb, and Fe/Co.

Figure 4a shows typical EDS spectra of the $Ce_xFe_3CoSb_{12}$. All samples are composed of Ce, Fe, Co, and Sb without other impurity elements. Figure 4b shows the average atomic ratios of Fe, Co, Sb, and Ce elements in each sample based on the statistic EDS results. As can be seen, the Ce-filling level in the samples increases at first and then tends to be stabilized at the x of 1.25, which is consistent with the peak shift from XRD. Figure 4c compares the Ce-filling fraction of Fe-doped $CoSb_3$ prepared by different methods. The Ce filling fraction varies with the preparation method and Fe/Co ratio. The Fe/Co ratio in the actual composition of the samples shown in the red dotted box in Figure 4c is close to ~2.5. Under the similar Fe/Co ratio, a relative high filling fraction of 0.73 is achieved in a composition of $Ce_{0.73}Fe_{2.73}Co_{1.18}Sb_{12}$ prepared by the TGZM method in this study. Figure 4d shows the TEM-EDS spectrum and maps of the $CeFe_3CoSb_{12}$. As can be seen, Fe, Co, Sb, and Ce elements are homogeneously distributed on a micro-scale, indicating successful Fe substitution at the Co site and Ce-filling.

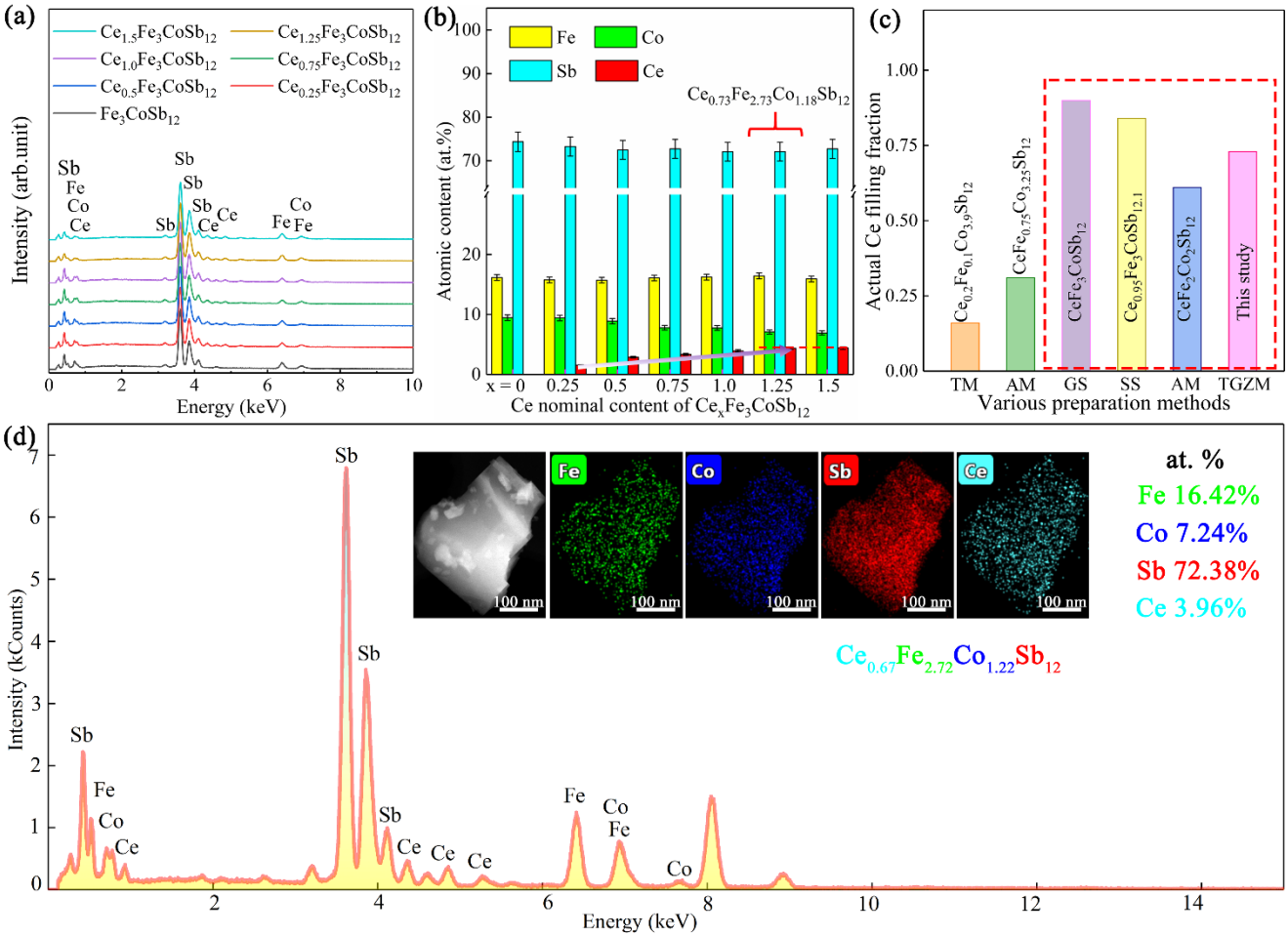

Figure 4. Detailed component information acquired by EDS: (**a**) EDS spectra and corresponding (**b**) average atomic ratios of Fe, Co, Sb, Ce elements in $Ce_xFe_3CoSb_{12}$ (x = 0 to 1.5) samples. (**c**) comparison of the Ce filling fraction in Fe-doped $CoSb_3$ prepared by different methods, including traditional melting (TM) for $Ce_{0.2}Fe_{0.1}Co_{3.9}Sb_{12}$, [58] arc melting (AM) for $CeFe_2Co_2Sb_{12}$ [59] and $CeFe_{0.75}Co_{3.25}Sb_{12}$ [39], gas-atomized powder sintering (GS) for $CeFe_3CoSb_{12}$, [45] scanning laser melting and spark plasma sintering (SS) for $Ce_{0.95}Fe_3CoSb_{12.1}$ [46] and temperature gradient zone melting (TGZM) for this study. (**d**) Typical TEM-EDS spectrum of the $CeFe_3CoSb_{12}$. The insert of (**d**) is the HAADF image, corresponding elemental maps and component analysis.

3.2. Thermoelectric Transport Properties

To understand the thermoelectric properties of the as-fabricated $Ce_xFe_3CoSb_{12}$ (x = 0 to 1.5), σ, S, $S^2\sigma$, and κ were measured at the temperature range between 303 and 813 K. Figure 5a depicts temperature-dependent σ of the $Ce_xFe_3CoSb_{12}$. The Fe_3CoSb_{12} has a higher σ (1302 S cm^{-1}) comparing with the Ce-filled samples in the entire measured temperature. With increasing the Ce-filling level, the σ of the $Ce_xFe_3CoSb_{12}$ decreases from 1302 S cm^{-1} of the Fe_3CoSb_{12} to 638 S cm^{-1} of the $Ce_{1.25}Fe_3CoSb_{12}$ at 303 K. The slight increase of σ from x = 1.25 to 1.5 might be attributed to the slightly increased Sb content (as evidenced by the XRD peak intensity in Figure 2a). Besides, the nearly linear decrease of σ with increasing the temperature indicates that the as-fabricated $Ce_xFe_3CoSb_{12}$ is a degenerated semiconductor. With increasing the Ce content, S increases from 62 μV K^{-1} of the Fe_3CoSb_{12} to 117 μV K^{-1} of the $Ce_{1.25}Fe_3CoSb_{12}$ at 303 K (Figure 5b). The maximum S value of 168 μV K^{-1} at 693 K can be obtained in the $Ce_{1.25}Fe_3CoSb_{12}$. The positive S indicates that the $Ce_xFe_3CoSb_{12}$ is p-type, which is consistent with the calculation of the band structures. A classic single parabolic band (SPB) model was used to evaluate the effective mass m^* as described by Equations (1)–(4) [18,60]:

$$S = \pm\frac{k_B}{e}\left(\frac{2F_1(\eta)}{F_0(\eta)} - \eta\right) \tag{1}$$

$$m^* = \frac{h^2}{2k_BT}\left[\frac{nr_H}{4\pi F_{1/2}(\eta)}\right] \tag{2}$$

$$r_H = \frac{3}{2}\frac{F_{1/2}(\eta)F_{-1/2}(\eta)}{2F_0^2(\eta)} \tag{3}$$

$$F_n(\eta) = \int_0^\infty \frac{x^n}{1+e^{x-\eta}}\mathrm{d}x \tag{4}$$

where e is the electron charge, η the reduced Fermi energy, $\eta = E_F/k_BT$, $F_n(\eta)$ the Fermi integral and r_H the Hall factor. Figure 5c shows the Pisarenko plot of Fe_3CoSb_{12} with the measured room-temperature n_H and corresponding S of Ce-filled Fe_3CoSb_{12} samples. With increasing Ce-filling level, the experimental S values corresponding to the n_H deviates from the Pisarenko plot to a higher level, indicating that Ce-filling led to an increase of the m^*. This should be attributed to the increased DOS near the edge of the band structure (Figure 1e,f) induced by Ce-filling. The maximum $S^2\sigma$ (Figure 5d) significantly increases from 6.7 μW cm^{-1} K^{-2} of the Fe_3CoSb_{12} to 14.4 μW cm^{-1} K^{-2} of the $Ce_{1.25}Fe_3CoSb_{12}$ at 693 K.

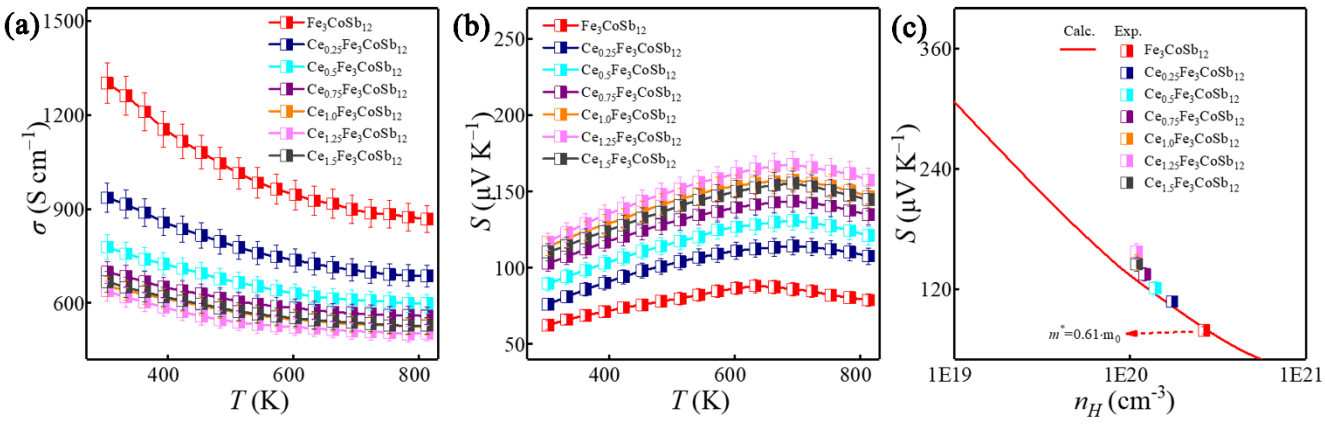

Figure 5. *Cont.*

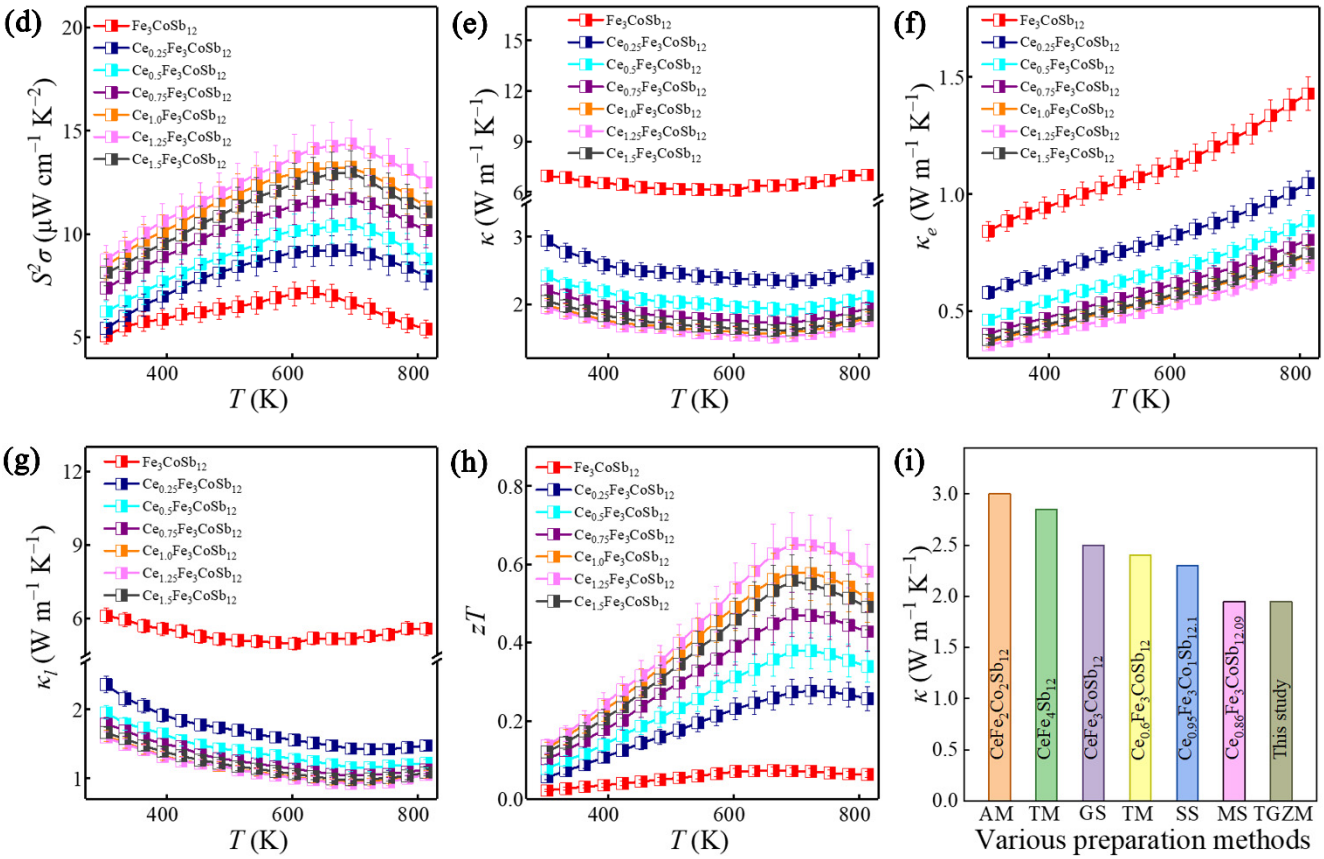

Figure 5. Thermoelectric properties of $Ce_xFe_3CoSb_{12}$ (x = 0 to 1.5). Temperature-dependent (**a**) σ; (**b**) S. (**c**) The experimental S values corresponding to the n_H, where the red line represents the Pisarenko plot for Fe_3CoSb_{12}. Temperature-dependent (**d**) $S^2\sigma$; (**e**) κ; (**f**) κ_e; (**g**) κ_l; (**h**) zT. (**i**) Comparison of the room-temperature κ for nominal $Ce_{1.25}Fe_3CoSb_{12}$ with the reported values for $CeFe_2Co_2Sb_{12}$ prepared by AM, [59] $CeFe_4Sb_{12}$ [61] and $Ce_{0.6}Fe_3CoSb_{12}$ [62] prepared by TM, $CeFe_3CoSb_{12}$ prepared by GS, [45] $Ce_{0.95}Fe_3CoSb_{12.1}$ prepared by SS, [46] and $Ce_{0.86}Fe_3CoSb_{12.09}$ prepared by melt spinning and spark plasma sintering (MS) [63].

Figure 5e plots temperature-dependent κ of the as-fabricated $Ce_xFe_3CoSb_{12}$ (x = 0 to 1.5). With increasing the Ce-filling level, the κ gradually decreases and approaches 1.52 W m^{-1} K^{-1} of $Ce_{1.25}Fe_3CoSb_{12}$ at 693 K. The κ_e can be calculated as $\kappa_e = L\sigma T$ (Figure 5f), where L is the Lorenz number calculated based on SPB model. With increasing the Ce-filling level, the κ_e significantly reduces due to reduced σ. Figure 5g presents temperature-dependent κ_l, calculated by κ-κ_e. The κ_l of the Ce-filled Fe_3CoSb_{12} is much lower than that of the unfilled Fe_3CoSb_{12}. The k_l reduces with increasing the Ce-filling level and approaches a lowest κ_l of 0.91 W m^{-1} K^{-1} at 693 K in the $Ce_{1.25}Fe_3CoSb_{12}$. This should be primarily attributed to the rattling effect for strengthening short-wavelength phonon scattering, induced by Ce-filling [64]. Figure 5h displays temperature-dependent zT of the as-fabricated $Ce_xFe_3CoSb_{12}$ (x = 0 to 1.5). Benefitting from the enhanced $S^2\sigma$ and significantly reduced k, a peak zT value of 0.65 can be achieved in the $Ce_{1.25}Fe_3CoSb_{12}$ at 693 K, which is 9 times higher than that of the unfilled Fe_3CoSb_{12}. Figure 5i compares the room-temperature κ of nominal $Ce_{1.25}Fe_3CoSb_{12}$ in this study prepared by TGZM with the reported κ of p-type Ce-filled and Fe-doped $CoSb_3$ prepared by other methods. As can be seen, a relatively lower κ is obtained in TGZM prepared $Ce_{1.25}Fe_3CoSb_{12}$, which is due to the higher Ce filling fraction with an optimized Fe/Co ratio. Besides, the maximum zT values of different Ce-filled and Fe-doped $CoSb_3$ prepared by various methods are compared and shown in Figure S1 of the Supplementary Material, indicating a higher zT value can be obtained by optimizing Ce-filling fraction and Fe/Co ratio.

4. Conclusions

In this study, under the guidance of the DFT calculation, where Ce-filling can introduce an impurity level near the E_F and increase the thermoelectric performance of the Fe_3CoSb_{12}, we have designed and prepared the p-type $Ce_xFe_3CoSb_{12}$ (x = 0 to 1.5) by a facile TGZM method. The Ce-filling limit in TGZM-prepared Fe_3CoSb_{12} was found to be 0.73 with a measured composition of $Ce_{0.73}Fe_{2.73}Co_{1.18}Sb_{12}$. The filling limit is approached at the nominal composition of $Ce_{1.25}Fe_3CoSb_{12}$. Under the synergistic effect, Fe substitution at the Co site and Ce-filling, an optimal n_H of 1.03×10^{20} cm^{-3} is approached. The high S of 168 μV K^{-1} at 693 K due to the increase of the Ce filling level induces a high $S^2\sigma$ of 14.4 μW cm^{-1} K^{-2} at 693 K in the $Ce_{1.25}Fe_3CoSb_{12}$, which is increased by 100% comparing with that of the Fe_3CoSb_{12}. The rattling effect of Ce fillers strongly strengthens phonon scattering, leading to reduced κ_l as low as 0.91 W m^{-1} K^{-1} at 693 K in the $Ce_{1.25}Fe_3CoSb_{12}$. Benefiting from the low κ of 1.52 W m^{-1} K^{-1} induced by both optimized n_H and reduced κ_l, a peak zT value of 0.65 at 693 K can be achieved in the $Ce_{1.25}Fe_3CoSb_{12}$, which is 9 times higher than the Fe_3CoSb_{12}.

Supplementary Materials: The following are available online at https://www.mdpi.com/article/10.3390/ma14226810/s1, Comparison of the maximum zT value of nominal $Ce_{1.25}Fe_3CoSb_{12}$ in this study prepared by TGZM with the reported zT of p-type Ce-filled and Fe-doped $CoSb_3$ prepared by other methods.

Author Contributions: Conceptualization, X.-G.L., D.L. and S.-M.L.; methodology, X.-G.L. and W.-D.L.; software, X.-G.L., D.L. and B.Y.; validation, X.-G.L., W.-D.L. and S.-M.L.; formal analysis, X.-G.L., B.Y. and J.-X.Z.; investigation, X.-G.L., J.-X.Z. and Z.-Y.F.; resources, S.-M.L.; data curation, H.Z. and Z.-Y.F.; writing—original draft preparation, X.-G.L., W.-D.L. and X.-L.S.; writing—review and editing, S.-M.L., X.-L.S. and Z.-G.C.; supervision, H.Z.; project administration, S.-M.L. and W.-D.L.; funding acquisition, S.-M.L. and Z.-G.C. All authors have read and agreed to the published version of the manuscript.

Funding: This work was financially supported by the National Natural Science Foundation of China (NO.51774239), Australian Research Council and HBIS-UQ Innovation Centre for Sustainable Steel (ICSS) project.

Institutional Review Board Statement: Not applicable.

Informed Consent Statement: Not applicable.

Data Availability Statement: The data presented in this study are available upon request from the corresponding author.

Acknowledgments: We would like to thank the Analytical & Testing Center of Northwestern Polytechnical University for the measurement of XRD, SEM and TEM.

Conflicts of Interest: The authors declare no conflict of interest.

References

1. Yan, Y.; Ke, H.; Yang, J.; Uher, C.; Tang, X. Fabrication and Thermoelectric Properties of n-Type $CoSb_{2.85}Te_{0.15}$ Using Selective Laser Melting. *ACS Appl. Mater. Inter.* **2018**, *10*, 13669–13674. [CrossRef]
2. Qin, B.; Wang, D.; Liu, X.; Qin, Y.; Dong, J.F.; Luo, J.; Li, J.W.; Liu, W.; Tan, G.; Tang, X.; et al. Power generation and thermoelectric cooling enabled by momentum and energy multiband alignments. *Science* **2021**, *373*, 556–561. [CrossRef] [PubMed]
3. Roychowdhury, S.; Ghosh, T.; Arora, R.; Samanta, M.; Xie, L.; Singh, N.K.; Soni, A.; He, J.; Waghmare, U.V.; Biswas, K. Enhanced atomic ordering leads to high thermoelectric performance in $AgSbTe_2$. *Science* **2021**, *371*, 722–727. [CrossRef]
4. Shi, X.L.; Zou, J.; Chen, Z.G. Advanced Thermoelectric Design: From Materials and Structures to Devices. *Chem. Rev.* **2020**, *120*, 7399–7515. [CrossRef]
5. Snyder, G.J.; Toberer, E.S. Complex thermoelectric materials. *Nat. Mater.* **2008**, *7*, 105. [CrossRef] [PubMed]
6. Meng, X.; Cai, W.; Liu, Z.; Li, J.; Geng, H.; Sui, J. Enhanced thermoelectric performance of p-type filled skutterudites via the coherency strain fields from spinodal decomposition. *Acta Mater.* **2015**, *98*, 405–415. [CrossRef]
7. Hong, M.; Lyu, W.; Wang, Y.; Zou, J.; Chen, Z.G. Establishing the Golden Range of Seebeck Coefficient for Maximizing Thermoelectric Performance. *J. Am. Chem. Soc.* **2020**, *142*, 2672–2681. [CrossRef] [PubMed]

8. Wang, Y.; Hong, M.; Liu, W.D.; Shi, X.L.; Xu, S.D.; Sun, Q.; Gao, H.; Lu, S.; Zou, J.; Chen, Z.G. $Bi_{0.5}Sb_{1.5}Te_3$/PEDOT:PSS-based flexible thermoelectric film and device. *Chem. Eng. J.* **2020**, *397*, 125360. [CrossRef]
9. Shi, X.L.; Wu, H.; Liu, Q.; Zhou, W.; Lu, S.; Shao, Z.; Dargusch, M.; Chen, Z.G. $SrTiO_3$-based thermoelectrics: Progress and challenges. *Nano Energy* **2020**, *78*, 105195. [CrossRef]
10. Ghosh, S.; Shankar, G.; Karati, A.; Werbach, K.; Rogl, G.; Rogl, P.; Bauer, E.; Murty, B.S.; Suwas, S.; Mallik, R.C. Enhanced Thermoelectric Performance in the $Ba_{0.3}Co_4Sb_{12}$/InSb Nanocomposite Originating from the Minimum Possible Lattice Thermal Conductivity. *ACS Appl. Mater. Inter.* **2020**, *12*, 48729–48740. [CrossRef]
11. Ji, W.; Shi, X.L.; Liu, W.D.; Yuan, H.; Zheng, K.; Wan, B.; Shen, W.; Zhang, Z.; Fang, C.; Wang, Q.; et al. Boosting the thermoelectric performance of n-type Bi_2S_3 by hierarchical structure manipulation and carrier density optimization. *Nano Energy* **2021**, *87*, 106171. [CrossRef]
12. Liu, T.; Chen, J.; Li, M.; Han, G.; Liu, C.; Zhou, D.; Zou, J.; Chen, Z.G.; Yang, L. Achieving enhanced thermoelectric performance of $Ca_{1-x-y}La_xSr_yMnO_3$ via synergistic carrier concentration optimization and chemical bond engineering. *Chem. Eng. J.* **2021**, *408*, 127364. [CrossRef]
13. Fang, T.; Zhao, X.; Zhu, T. Band Structures and Transport Properties of High-Performance Half-Heusler Thermoelectric Materials by First Principles. *Materials* **2018**, *11*, 847. [CrossRef]
14. Wu, H.; Shi, X.L.; Liu, W.D.; Li, M.; Gao, H.; Zhou, W.; Shao, Z.; Wang, Y.; Liu, Q.; Chen, Z.G. Double perovskite Pr_2CoFeO_6 thermoelectric oxide: Roles of Sr-doping and Micro/nanostructuring. *Chem. Eng. J.* **2021**, *425*, 130668. [CrossRef]
15. Zhou, C.; Yu, Y.; Lee, Y.L.; Ge, B.; Lu, W.; Cojocaru-Mirédin, O.; Im, J.; Cho, S.P.; Wuttig, M.; Shi, Z.; et al. Exceptionally High Average Power Factor and Thermoelectric Figure of Merit in n-type PbSe by the Dual Incorporation of Cu and Te. *J. Am. Chem. Soc.* **2020**, *142*, 15172–15186. [CrossRef] [PubMed]
16. Zheng, Z.H.; Shi, X.L.; Ao, D.W.; Liu, W.D.; Chen, Y.X.; Li, F.; Chen, S.; Tian, X.Q.; Li, X.R.; Duan, J.Y.; et al. Rational band engineering and structural manipulations inducing high thermoelectric performance in n-type $CoSb_3$ thin films. *Nano Energy* **2021**, *81*, 105683. [CrossRef]
17. Choi, S.; Kurosaki, K.; Harnwunggmoung, A.; Miyazaki, Y.; Ohishi, Y.; Muta, H.; Yamanaka, S. Enhancement of thermoelectric properties of $CoSb_3$ skutterudite by addition of Ga and In. *Jpn. J. Appl. Phys.* **2015**, *54*, 111801. [CrossRef]
18. Meng, X.; Liu, Y.; Cui, B.; Qin, D.; Cao, J.; Liu, W.; Liu, Z.; Cai, W.; Sui, J. High thermoelectric performance of single phase p-type cerium-filled skutterudites by dislocation engineering. *J. Mater. Chem. A* **2018**, *6*, 20128–20137. [CrossRef]
19. Zhang, Q.; Zhou, Z.; Dylla, M.; Agne, M.T.; Pei, Y.; Wang, L.; Tang, Y.; Liao, J.; Li, J.; Bai, S.; et al. Realizing high-performance thermoelectric power generation through grain boundary engineering of skutterudite-based nanocomposites. *Nano Energy* **2017**, *41*, 501–510. [CrossRef]
20. Ghosh, S.; Meledath Valiyaveettil, S.; Shankar, G.; Maity, T.; Chen, K.-H.; Biswas, K.; Suwas, S.; Mallik, R.C. Enhanced Thermoelectric Properties of In-Filled Co_4Sb_{12} with InSb Nanoinclusions. *ACS Appl. Energ. Mater.* **2020**, *3*, 635–646. [CrossRef]
21. Tan, G.; Chi, H.; Liu, W.; Zheng, Y.; Tang, X.; He, J.; Uher, C. Toward high thermoelectric performance p-type $FeSb_{2.2}Te_{0.8}$ via in situ formation of InSb nanoinclusions. *J. Mater. Chem. C* **2015**, *3*, 8372–8380. [CrossRef]
22. Bourgès, C.; Sato, N.; Baba, T.; Baba, T.; Ohkubo, I.; Tsujii, N.; Mori, T. Drastic power factor improvement by Te doping of rare earth-free $CoSb_3$-skutterudite thin films. *RSC Adv.* **2020**, *10*, 21129–21135. [CrossRef]
23. Wan, S.; Huang, X.; Qiu, P.; Shi, X.; Chen, L. Compound Defects and Thermoelectric Properties of Self-Charge Compensated Skutterudites $Se_yCo_4Sb_{12-x}Se_x$. *ACS Appl. Mater. Inter.* **2017**, *9*, 22713–22724. [CrossRef]
24. Yang, H.; Wen, P.; Zhou, X.; Li, Y.; Duan, B.; Zhai, P.; Zhang, Q. Enhanced thermoelectric performance of Te-doped skutterudite with nano-micro-porous architecture. *Scr. Mater.* **2019**, *159*, 68–71. [CrossRef]
25. Okamoto, H. Co-Sb (Cobalt-Antimony). *J. Phase Equilib. Diff.* **1991**, *12*, 244–245. [CrossRef]
26. Tang, Y.; Chen, S.W.; Snyder, G.J. Temperature dependent solubility of Yb in Yb–$CoSb_3$ skutterudite and its effect on preparation, optimization and lifetime of thermoelectrics. *J. Mater.* **2015**, *1*, 75–84. [CrossRef]
27. Aversano, F.; Branz, S.; Bassani, E.; Fanciulli, C.; Ferrario, A.; Boldrini, S.; Baricco, M.; Castellero, A. Effect of rapid solidification on the synthesis and thermoelectric properties of Yb-filled Co_4Sb_{12} skutterudite. *J. Alloy. Compd.* **2019**, *796*, 33–41. [CrossRef]
28. Rull-Bravo, M.; Moure, A.; Fernández, J.F.; Martín-González, M. Skutterudites as thermoelectric materials: Revisited. *RSC Adv.* **2015**, *5*, 41653–41667. [CrossRef]
29. Li, X.; Zhang, Q.; Kang, Y.; Chen, C.; Zhang, L.; Yu, D.; Tian, Y.; Xu, B. High pressure synthesized Ca-filled $CoSb_3$ skutterudites with enhanced thermoelectric properties. *J. Alloy. Compd.* **2016**, *677*, 61–65. [CrossRef]
30. Ortiz, B.R.; Crawford, C.M.; McKinney, R.W.; Parilla, P.A.; Toberer, E.S. Thermoelectric properties of bromine filled $CoSb_3$ skutterudite. *J. Mater. Chem. A* **2016**, *4*, 8444–8450. [CrossRef]
31. Slack, G.A. New Materials and Performance Limits for Thermoelectric Cooling. In *CRC Handbook of Thermoelectrics*; CRC Press: Boca Raton, FL, USA, 1995; pp. 407–440.
32. Zhang, S.; Xu, S.; Gao, H.; Lu, Q.; Lin, T.; He, P.; Geng, H. Characterization of multiple-filled skutterudites with high thermoelectric performance. *J. Alloy. Compd.* **2020**, *814*, 152272. [CrossRef]
33. Serrano-Sánchez, F.; Prado-Gonjal, J.; Nemes, N.M.; Biskup, N.; Varela, M.; Dura, O.J.; Martínez, J.L.; Fernández-Díaz, M.T.; Fauth, F.; Alonso, J.A. Low thermal conductivity in La-filled cobalt antimonide skutterudites with an inhomogeneous filling factor prepared under high-pressure conditions. *J. Mater. Chem. A* **2018**, *6*, 118–126. [CrossRef]

34. Li, W.; Wang, J.; Xie, Y.; Gray, J.L.; Heremans, J.J.; Kang, H.B.; Poudel, B.; Huxtable, S.T.; Priya, S. Enhanced Thermoelectric Performance of Yb-Single-Filled Skutterudite by Ultralow Thermal Conductivity. *Chem. Mater.* **2019**, *31*, 862–872. [CrossRef]
35. Kang, Y.; Yu, F.; Chen, C.; Zhang, Q.; Sun, H.; Zhang, L.; Yu, D.; Tian, Y.; Xu, B. High pressure synthesis and thermoelectric properties of Ba-filled $CoSb_3$ skutterudites. *J. Mater. Sci. Mater. Electron.* **2017**, *28*, 8771–8776. [CrossRef]
36. Pei, Y.Z.; Yang, J.; Chen, L.D.; Zhang, W.; Salvador, J.R.; Yang, J. Improving thermoelectric performance of caged compounds through light-element filling. *Appl. Phys. Lett.* **2009**, *95*, 042101. [CrossRef]
37. Zhou, Z.; Li, J.; Fan, Y.; Zhang, Q.; Lu, X.; Fan, S.; Kikuchi, K.; Nomura, N.; Kawasaki, A.; Wang, L.; et al. Uniform dispersion of SiC in Yb-filled skutterudite nanocomposites with high thermoelectric and mechanical performance. *Scr. Mater.* **2019**, *162*, 166–171. [CrossRef]
38. Ren, W.; Sun, Y.; Zhang, J.; Xia, Y.; Geng, H.; Zhang, L. Doping distribution in Skutterudites with ultra-high filling fractions for achieving ultra-low thermal conductivity. *Acta Mater.* **2021**, *209*, 116791. [CrossRef]
39. Morelli, D.T.; Meisner, G.P.; Chen, B.X.; Hu, S.Q.; Uher, C. Cerium filling and doping of cobalt triantimonide. *Phys. Rev. B* **1997**, *56*, 7376–7383. [CrossRef]
40. Tang, Y.; Hanus, R.; Chen, S.W.; Snyder, G.J. Solubility design leading to high figure of merit in low-cost Ce-$CoSb_3$ skutterudites. *Nat. Commun.* **2015**, *6*, 7584. [CrossRef]
41. Smalley, A.L.E.; Howe, B.; Johnson, D.C. The Synthesis of Ce-filled $CoSb_3$ and Characterization of its Magnetic and Structural Properties. In *Thermoelectric Materials 2003—Research and Applications*; MRS Proceedings: Cambridge, UK, 2004; Volume 793, pp. 413–418. [CrossRef]
42. Thompson, D.R.; Liu, C.; Yang, J.; Salvador, J.R.; Haddad, D.B.; Ellison, N.D.; Waldo, R.A.; Yang, J. Rare-earth free p-type filled skutterudites: Mechanisms for low thermal conductivity and effects of Fe/Co ratio on the band structure and charge transport. *Acta Mater.* **2015**, *92*, 152–162. [CrossRef]
43. Matsubara, M.; Masuoka, Y.; Asahi, R. Effects of doping IIIB elements (Al, Ga, In) on thermoelectric properties of nanostructured n-type filled skutterudite compounds. *J. Alloy. Compd.* **2019**, *774*, 731–738. [CrossRef]
44. Son, G.; Lee, K.H.; Park, H.-W.; Caron, A.; Kim, I.H.; Lee, S.; Choi, S.M. Control of electrical to thermal conductivity ratio for p-type $La_xFe_3CoSb_{12}$ thermoelectrics by using a melt-spinning process. *J. Alloy. Compd.* **2017**, *729*, 1209–1214. [CrossRef]
45. Tanahashi, H.; Ohta, Y.; Uchida, H.; Itsumi, Y.; Kasama, A.; Matsubara, K. Formation of cerium-filled skutterudite thermoelectric materials in the sintering of gas-atomized powder. *J. Jpn. Inst. Metals* **2001**, *65*, 955–960. [CrossRef]
46. Chen, F.; Liu, R.; Yao, Z.; Xing, Y.; Bai, S.; Chen, L. Scanning laser melting for rapid and massive fabrication of filled skutterudites with high thermoelectric performance. *J. Mater. Chem. A* **2018**, *6*, 6772–6779. [CrossRef]
47. Bhardwaj, R.; Johari, K.K.; Gahtori, B.; Chauhan, N.S.; Bathula, S.; Dhakate, S.R.; Auluck, S.; Dhar, A. Optimization of electrical and thermal transport properties of $Fe_{0.25}Co_{0.75}Sb_3$ Skutterudite employing the isoelectronic Bi-doping. *Intermetallics* **2020**, *123*, 106796. [CrossRef]
48. Shi, X.; Wu, A.; Feng, T.; Zheng, K.; Liu, W.; Sun, Q.; Hong, M.; Pantelides, S.T.; Chen, Z.G.; Zou, J. High Thermoelectric Performance in p-type Polycrystalline Cd-doped SnSe Achieved by a Combination of Cation Vacancies and Localized Lattice Engineering. *Adv. Energy Mater.* **2019**, *9*, 1803242. [CrossRef]
49. Yu, J.; Zhu, W.T.; Zhao, W.Y.; Luo, Q.; Liu, Z.Y.; Chen, H. Rapid fabrication of pure p-type filled skutterudites with enhanced thermoelectric properties via a reactive liquid-phase sintering. *J. Mater. Sci.* **2020**, *55*, 7432–7440. [CrossRef]
50. Lee, S.; Lee, K.H.; Kim, Y.M.; Kim, H.S.; Snyder, G.J.; Baik, S.; Kim, S.W. Simple and efficient synthesis of nanograin structured single phase filled skutterudite for high thermoelectric performance. *Acta Mater.* **2018**, *142*, 8–17. [CrossRef]
51. Jie, Q.; Wang, H.; Liu, W.; Wang, H.; Chen, G.; Ren, Z. Fast phase formation of double-filled p-type skutterudites by ball-milling and hot-pressing. *Phys. Chem. Chem. Phys.* **2013**, *15*, 6809–6816. [CrossRef]
52. Li, X.; Li, S.; Li, D.; Yang, B.; Xu, C.; Zhong, H. Effect of hot pressing on the microstructure and thermoelectric properties of TGZM-grown YbFe-doped $CoSb_3$ skutterudite. *Ceram. Int.* **2021**, *47*, 8949–8958. [CrossRef]
53. Li, D.; Li, S.; Li, X.; Yang, B.; Zhong, H. Efficiently synthesized n-type $CoSb_3$ thermoelectric alloys under TGZM effect. *Mater. Sci. Semicond. Process.* **2021**, *123*, 105542. [CrossRef]
54. Peng, P.; Zhang, X.; Xu, Y.; Li, Y.; Yang, J.; Zhang, A.; Yue, J. Liquid migration and peritectic transformation: Investigation on their contributions to growth of peritectic phase in interrupted directional solidification. *Int. Commun. Heat Mass* **2020**, *118*, 104888. [CrossRef]
55. Löffler, A.; Reuther, K.; Engelhardt, H.; Liu, D.; Rettenmayr, M. Resolidification of the mushy zone of multiphase and multicomponent alloys in a temperature gradient—Experiments and modeling. *Acta Mater.* **2015**, *91*, 34–40. [CrossRef]
56. Lu, P.X.; Ma, Q.H.; Li, Y.; Hu, X. A study of electronic structure and lattice dynamics of $CoSb_3$ skutterudite. *J. Magn. Magn. Mater.* **2010**, *322*, 3080–3083. [CrossRef]
57. Kholil, M.I.; Bhuiyan, M.T.H. Elastic, electronic, vibrational and optical properties of filled skutterudite compound $SrRu_4As_{12}$: Insights from DFT-based computer simulation. *Comput. Condens. Matter.* **2021**, *26*, e00519. [CrossRef]
58. Qiu, P.; Shi, X.; Qiu, Y.; Huang, X.; Wan, S.; Zhang, W.; Chen, L.; Yang, J. Enhancement of thermoelectric performance in slightly charge-compensated $Ce_yCo_4Sb_{12}$ skutterudites. *Appl. Phys. Lett.* **2013**, *103*, 062103. [CrossRef]
59. Chen, B.X.; Xu, J.H.; Uher, C.; Morelli, D.T.; Meisner, G.P.; Fleurial, J.P.; Caillat, T.; Borshchevsky, A. Low-temperature transport properties of the filled skutterudites $CeFe_{4-x}Co_xSb_{12}$. *Phys. Rev. B* **1997**, *55*, 1476–1480. [CrossRef]

60. Tan, G.; Zhao, L.-D.; Kanatzidis, M.G. Rationally Designing High-Performance Bulk Thermoelectric Materials. *Chem. Rev.* **2016**, *116*, 12123–12149. [CrossRef]
61. Tan, G.; Liu, W.; Wang, S.; Yan, Y.; Li, H.; Tang, X.; Uher, C. Rapid preparation of $CeFe_4Sb_{12}$ skutterudite by melt spinning: Rich nanostructures and high thermoelectric performance. *J. Mater. Chem. A* **2013**, *1*, 12657–12668. [CrossRef]
62. Tan, G.J.; Wang, S.Y.; Tang, X.F. Thermoelectric Performance Optimization in p-Type $Ce_yFe_3CoSb_{12}$ Skutterudites. *J. Electron. Mater.* **2014**, *43*, 1712–1717. [CrossRef]
63. Bae, S.H.; Lee, K.H.; Choi, S.-M. Effective role of filling fraction control in p-type $Ce_xFe_3CoSb_{12}$ skutterudite thermoelectric materials. *Intermetallics* **2019**, *105*, 44–47. [CrossRef]
64. Shiota, Y.; Ohishi, Y.; Matsuda, M.; Shimada, T.; Nambu, A.; Muta, H. Improvement of thermoelectric property in Ce filled $Fe_3Co_1Sb_{12}$ by Sn addition. *J. Alloy. Compd.* **2020**, *829*, 154478. [CrossRef]